Green Chemistry

PAPER

View Article Online
View Journal | View Issue



Cite this: *Green Chem.*, 2026, **28**, 5259

# Sustainable photoredox C($sp^3$)–P bond formation *via* nitrogen-vacancy-engineered carbon nitride

Barbaros Bolat, [a] Melek Sermin Ozer, [a] Kang Sun,[b] Hai-Long Jiang, [b] Zafer Eroglu *[a] and Onder Metin *[a,c]

Selective construction of C($sp^3$)–P bonds remain a fundamental challenge in green chemistry due to the widespread use of transition-metals, peroxides, or stoichiometric oxidants in state-of-the-art methodologies. Here, we report a metal-free, selective and sustainable strategy for oxidative C($sp^3$)–P bond formation using nitrogen-vacancy-engineered carbon nitride (Nv-CN) photocatalysts. A series of Nv-CN were synthesized by thermal annealing of pristine CN under controlled temperatures and atmospheres, revealing a clear structure–defect–activity relationship that correlates nitrogen vacancies with their enhanced photocatalytic performance. Among them, cyanamide-based Nv-CN annealed at 650 °C under argon atmosphere, Nv-CN(C)-650Ar, demonstrated the highest photocatalytic activity in the photoredox C($sp^3$)–P bond formation, achieving up to 92% yield within 1 hour under blue LED irradiation at room temperature, outperforming previously reported photocatalytic systems. Structural analyses revealed that the superior performance of Nv-CN(C)-650Ar is closely linked to an optimized N-vacancy concentration and favorable material properties, including a highly disordered structure, increased $-NH_x$ functionalities, and a high density of paramagnetic defects. The photocatalyst also exhibits a porous architecture, large surface area, strong visible-light absorption, a narrowed bandgap, and suppressed charge recombination due to the mid-gap states. Mechanistic studies indicate a single-electron oxidation pathway mediated by superoxide radicals. Nv-CN(C)-650Ar demonstrates broad substrate scope, excellent stability, and reusability over five consecutive cycles. For the optimized model C–P bond formation on a 0.25 mmol scale, the *E*-factor was calculated to be $E$ = 1.4 by excluding the recyclable solvents. This work not only fills a critical gap in green C($sp^3$)–P bond formation, but also introduces the vacancy-performance relation through mechanistic understanding of defect engineering in CN materials and offers a sustainable, metal-free photocatalytic strategy for C–H functionalization.

Received 21st November 2025,
Accepted 24th February 2026

DOI: 10.1039/d5gc06242j

rsc.li/greenchem



## Green foundation

1. This work advances green chemistry by developing a metal- and oxidant-free photocatalytic strategy for visible-light-driven oxidative C($sp^3$)–P bond formation under mild conditions.
2. The presented photocatalytic strategy offers a sustainable alternative to current precious-metal catalysts, peroxides, and energy-intensive methods, enabling greener C($sp^3$)–H functionalization with an *E*-factor of 1.4 through a using reusable heterogeneous photocatalyst composed of solely C, N and H.
3. This work establishes a clear structure–defect–activity relationship, identifying nitrogen vacancies as a key design element for achieving high efficiency and selectivity in carbon nitride photocatalysts for C($sp^3$)–P bond formation. Integrating this methodology into continuous flow photoreactors could reduce solvent use, improve scalability, and accelerate industrial translation.

## Introduction

Over the last two decades, sustainable C($sp^3$)–H bond functionalization has emerged as a powerful synthetic strategy for constructing C–X (X = C, N, P, *etc.*) bonds under energy-efficient and atom-economic conditions while minimizing waste generation.[1–3] Tertiary amines bearing accessible α-C ($sp^3$)–H bonds are frequently investigated in this context due to their prevalence in biologically active scaffolds.[4] Among the

[a]*Department of Chemistry, College of Sciences, Koç University, 34450 Istanbul, Türkiye. E-mail: zeroglu@ku.edu.tr, ometin@ku.edu.tr*
[b]*Hefei National Research Center for Physical Sciences at the Microscale, Department of Chemistry, University of Science and Technology of China, 230026 Hefei, People's Republic of China*
[c]*Koç University Surface Science and Technology Center (KUYTAM), 34450 Istanbul, Türkiye*

various C–X bond forming reactions, C($sp^3$)–P bond construction *via* oxidative coupling of tertiary amines with phosphorus-based nucleophiles, particularly P(v)-containing heterocycles, has emerged as a valuable strategy due to its directness and utility in synthesizing key intermediates for medicinal chemistry, flame retardants,[5] and advanced materials.[6–9] Constructing stable C($sp^3$)–P bonds, with typical bond energies of *ca.* 272 kJ $mol^{-1}$,[10] has traditionally rely on classical methods such as Michaelis–Arbuzov, Pudovik, Abramov, Kabachnik–Fields, Michael, and Aza-Henry type additions, those suffer from poor sustainability profiles.[11,12] Conventional approaches typically form C–P bonds either by coupling C($sp^3$)–H bonds with organophosphorus nucleophiles[13–15] or by generating P-centered radicals.[16,17] These transformations often require transition-metal catalysts or photo-/electrochemical systems and primarily proceed through the nucleophilic addition of phosphorus species to intermediates such as iminium ions, aldehydes, allylic or benzylic cations, or through radical addition of P-centered species to enolates[18] and alkenes.[19] Moreover, the most current methods also rely on precious metal catalysts,[20] strong oxidants,[21,22] or elevated temperatures that limit their scalability, selectivity, and environmental compatibility.[23,24] Even current photocatalytic approaches employ ZnO, $TiO_2$,[15] Ru[25] or Pd-based[26] photocatalysts that either employ catalyst loadings of 1–10% to introduce metal waste, require higher energy input for exceeding 6–24 hours, or limited reusability.[27–31] Therefore, the development of metal-free, reusable, and visible-light-driven photocatalysts prepared under sustainable conditions for such oxidative C($sp^3$)–P coupling remains an ongoing challenge in the current literature, where various C–P bond formations are commonly performed by transition metal catalysts with moderate yields.[17,32]

In response to this challenge, two-dimensional (2D) semiconductors composed of earth-abundant elements such as carbon, nitrogen, and phosphorus have emerged as promising photocatalysts owing to their tunable structures, favorable optoelectronic properties, and intrinsic sustainability.[33–35] Among these, graphitic carbon nitride (CN) stands out for its metal-free semiconducting properties, broad visible light absorption around 2.7 eV, and high thermal and chemical stability.[36–39] Structurally, CN is formed by π-conjugated heptazine (tri-*s*-triazine) units linked by $sp^2$-hybridized C and N atoms, along with H terminations, forming a layered framework held together by van der Waals forces.[40] The band structure of CN makes it a suitable semiconductor for a wide range of photoredox transformations.[41] Nevertheless, pristine CN suffers from major drawbacks, including low surface area (<10 $m^2$ $g^{-1}$), limited charge mobility, and high electron–hole recombination rates that restrict the effectiveness of CN in challenging organic photocatalysis.[42–45] To overcome these limitations, researchers have explored a variety of strategies, including chemical doping,[46,47] heterojunction formation,[48,49] structural functionalizations,[50,51] and defect engineering,[52–54] which are also discussed previously by our group in a review article.[55] The defect engineering strategies with particular focus on generating nitrogen vacancies (Nv) through controlled annealing are one of the most effective approaches to enhance the photocatalytic performance of CN.[56,57] These vacancies introduce mid-gap states that can modify the band structure and charge carrier mobility, increase the specific surface area, and enhance the light absorption, while also serving as active sites or charge carrier traps that improve separation efficiency.[58,59] Furthermore, Nv-engineering enables selective tuning of redox potential and surface polarity, which are highly important for photocatalytic applications.

Despite extensive efforts dedicated to defect engineering strategies,[55] current studies largely fall short in systematic and mechanistic understanding for the relationship between CN precursors, the conditions favoring Nv formation, and their impact on structure–activity correlation. On the other hand, from an application-oriented perspective, although there are examples of Nv-CN materials for various photocatalytic applications including water splitting,[60] carbon dioxide reduction,[61] wastewater treatment,[62] and photoredox organic transformations,[63,64] the synergistic interplay between Nv and mid-gap states in driving photooxidation reactions within organophosphorus chemistry remains still a subject of active discussion.

To address the knowledge gap in defect engineering of carbon nitride and its impact on photocatalytic activity, while advancing an efficient and sustainable strategy for C($sp^3$)–P bond construction, we report herein the superior photocatalytic performance of nitrogen-vacancy-engineered carbon nitride (Nv-CN) in the C($sp^3$)–P bond formation. To get the best photocatalysts with the optimal Nv, a comprehensive and comparative systematic study on defect-engineered CN photocatalysts was performed by using three different nitrogen-rich precursors and varying thermal annealing conditions under different atmospheres. These parameters include the effects of (i) precursor choice as cyanamide, dicyandiamide, and melamine, (ii) annealing temperature as 600 °C and 650 °C, and (iii) annealing atmosphere as under nitrogen and argon on the structural, photophysical, and electrochemical properties, as well as photocatalytic activities. Comprehensive structural and photophysical characterization revealed enhanced visible-light absorption, improved charge separation, and favorable electronic alignment in the annealed materials compared to their pristine analogues. Among the synthesized CN materials, Nv-CN(C)-650Ar exhibited the highest photocatalytic efficiency, catalyzing the oxidative C–P bond formation between tertiary amines and organophosphorus compounds entirely metal-free and without peroxides, strong oxidants, or high temperatures, using only blue LED irradiation, with high yields and excellent selectivity. The remarkable activity of Nv-CN(C)-650Ar in the photoredox C–P bond formation was elucidated through in-depth structural and electronic analyses, supported by detailed mechanistic investigations. The optimized reaction conditions were successfully applied to six challenging substrates, yielding products in the range of 73–92% without the need for metal catalysts or hazardous oxidants. Furthermore, reusability studies confirmed the chemical and photostability of Nv-CN

 

(C)-650Ar, with no significant loss in activity observed over five consecutive cycles using a minimal catalyst amount. For the optimized model C–P bond formation on a 0.25 mmol scale, the *E*-factor was calculated to be $E = 1.4$ (excluding recyclable solvents), which represent an excellent value for a challenging synthetic transformation like C($sp^3$)–P bond formation.[65] Nevertheless, the solvents used in this study are comparably more sustainable rather than halogenated solvent systems and the *E*-factor underline the potential of Nv-CN(C)-650Ar as a green and low-waste photocatalyst. Hence, by establishing direct links between synthesis, vacancy engineering, and catalytic outcomes, this study provides a mechanistic and design-oriented pathway that supports green metal-free photocatalysis for sustainable C($sp^3$)–P bond formation.

## Experimental section

### Synthesis of CN(X) and Nv-CN(X)-TG derivatives

Pristine CN(X) materials (X = C, D, M) were synthesized *via* thermal condensation of three nitrogen-rich precursors: cyanamide (C), dicyandiamide (D), and melamine (M), each processed individually to yield the corresponding CN structures by a standardized method developed for urea (Fig. 1a).[66] In this procedure, 10 g of the selected precursor was grinded in a mortar to fine powder and placed into a quartz crucible, which was heated in a muffle furnace with the heating program consisting of heating up to 550 °C with 5 °C $min^{-1}$ heating rate and then maintaining the temperature for 4 hours. The crucible was naturally cooled down to room temperature. From each precursor, the obtained CN materials weighed 0.8, 5.4, and 4.4 grams and with 8%, 54%, and 44% for CN(C), CN(D), and CN(M), respectively.

For the annealing, 1 g of as-prepared pale-yellow powder of CN(X) derivatives was compactly placed in a quartz boat, covered, and placed in a horizontal quartz-tube oven. Each derivative was annealed at 600 and 650 °C for 2 hours under $N_2$ or Ar gas flow with a 2 °C $min^{-1}$ heating rate. The powders of varying colors from dark-yellow to orange were obtained, and the resulting materials were labeled as Nv-CN(X)-TG, where X denotes the starting precursor, T represents the annealing temperature, and G indicates the gas atmosphere. While the weights of the Nv-CN derivatives vary between 0.4–0.9 g, the most efficient photocatalyst, namely Nv-CN(C)-650Ar was obtained 0.42 g with 42% yield.

### Photoredox C–P bond formation

In a small vial with a stirring bar, the photocatalyst was dispersed in the solvent, which was gassed with $O_2$ gas prior to use. The mixture was sonicated for 30 minutes for the dispersion. Subsequently, 62.75 mg of compound **1** (0.25 mmol) and 58.00 mg of compound **2** (0.25 mmol) were added to the vial. The vial was placed in the ThalesNano PhotoCube System.[67] The ambient temperature was controlled by a chiller while the reaction occurs. After the mixture was stirred under blue LED for 1 h, 43.3 mg of 1,3-dinitrobenzene (0.25 mmol) was added as the internal standard. The mixture was filtered through a syringe filter, extracted with ethyl acetate, then concentrated with a rotary evaporator. The yields were calculated based on $^1$H-NMR ratios.

## Results & discussion

### Synthesis and characterization of materials

To elucidate the relationship between the nitrogen-rich precursors, annealing conditions, and photocatalytic activity in the defect engineering of CN, the synthesis of Nv-CN was carried out through various routes starting from diverse precursors and employing a range of processing conditions (Fig. 1a). Pristine CN(X) materials (X: C, D, M) were synthesized *via* thermal condensation of three different nitrogen-rich precursors-cyanamide (C), dicyandiamide (D), and melamine (M)-each heated independently to obtain the corresponding CN structures. The obtained yields were relatively high compared to conventional urea-based synthesis that underline the potential scale-up synthesis.

To introduce Nv, as-prepared CN(X) materials were further annealed at two selected temperatures (600 °C or 650 °C) under inert atmospheres (argon or nitrogen). The annealed materials were denoted as Nv-CN(X)-TG, where X indicates the starting precursor, while T and G denote the annealing temperature and gas type, respectively. From a sustainability perspective, the synthesis of Nv-CN photocatalysts presents several advantages. The preparation relies on well-known solvent-free thermal condensation and annealing processes to avoid the use of toxic solvents, purification steps, or hazardous reagents. Hence, the generation of chemical waste is minimal and primarily limited to gaseous by-products such as ammonia that suggests a low *E*-factor compared to solution-processed or metal-containing photocatalysts. The versatile use of earth-abundant, low-cost nitrogen-rich precursors also improves economic feasibility and supports scalability. Although thermal treatment contributes to the overall energy input and carbon footprint, the drawback is neutralized by the high synthesis yields and the long-term stability and reusability of the catalyst.

X-ray diffraction (XRD) patterns of pristine CN(X) and Nv-CN(X)-TG derivatives were thoroughly investigated to elucidate their crystalline structures (Fig. 1b and Fig. S1) and to assess changes induced by defect engineering. The XRD patterns of all photocatalysts exhibited two diffraction peaks. While the major diffraction peak appears at $2\theta = 27.2°$ corresponding to the (002) plane due to the interplanar stacking of the conjugated π-system of CN sheets, the minor peak observed at $2\theta = 12.9°$ corresponds to the (100) plane due to the intraplanar repeating motifs of heptazine units.[40] Although the major (002) diffraction peak is preserved in all samples, shrinking of the (100) plane in Nv-CN(X)-TG derivatives suggests the loss of periodicity due to the partial breakdown of heptazine units during defect engineering.[68]

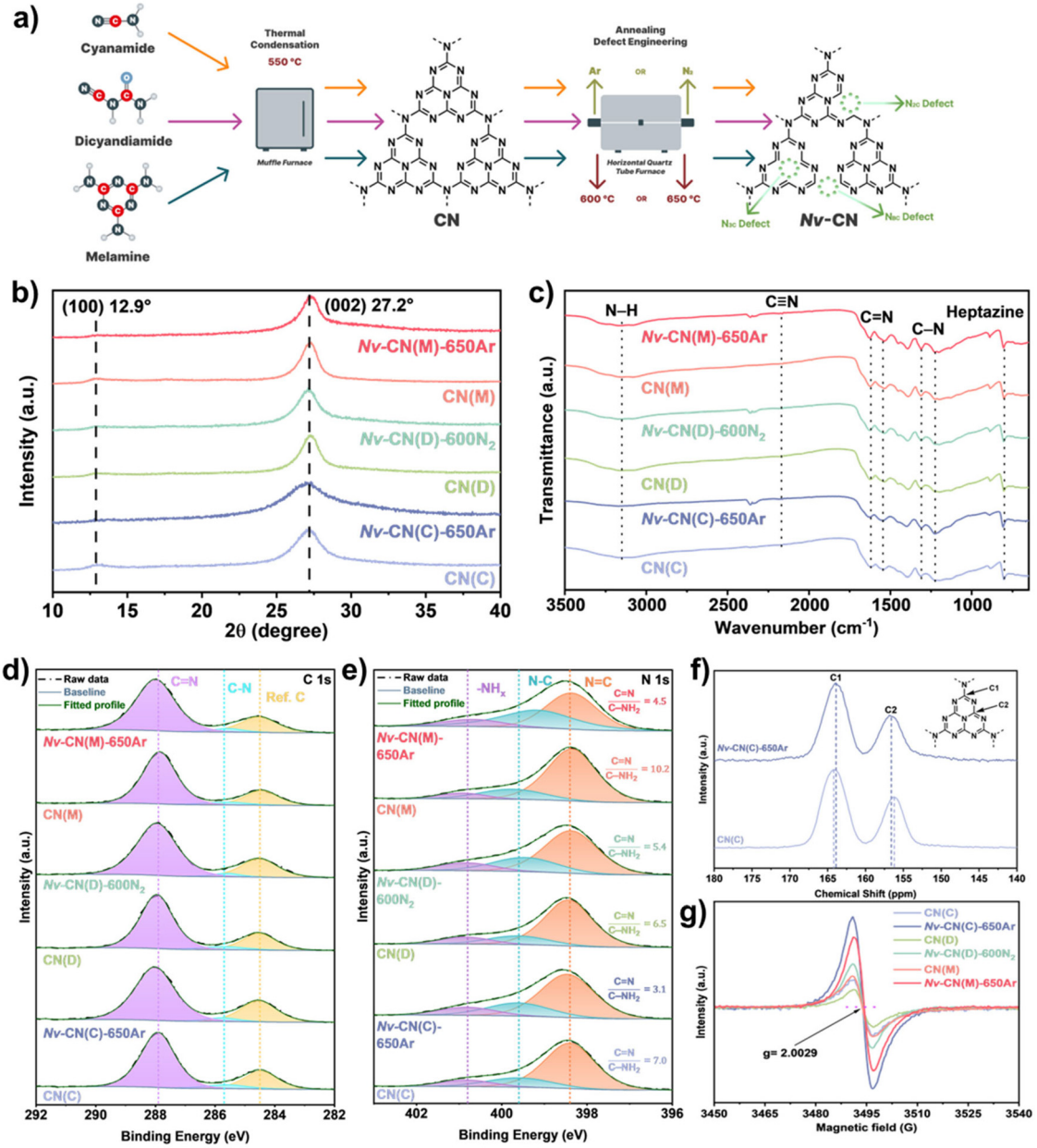


**Fig. 1** (a) The synthesis procedure, (b) XRD pattern, (c) FT-IR spectra, high-resolution (d) C 1s, (e) N 1s XPS spectra, (f) $^{13}C$ CP MAS NMR spectra, and (g) EPR spectra of CN-based materials.

To examine the generated functional groups, present in the synthesized materials and their changes during the annealing process, Fourier-transform infrared spectroscopy (FT-IR) was performed (Fig. 1c and Fig. S2). The sharp peak observed at 804 $cm^{-1}$ was assigned to the out-of-plane bending vibration of the heptazine ring, which is also known as the breathing mode.[69] While a set of peaks in the 1200–1400 $cm^{-1}$ region corresponds to the C–N and C–NH bond vibrations within the heptazine rings of the two-dimensional layers, a subsequent set of peaks in the 1400–1600 $cm^{-1}$ region corresponds to imine like-C=N vibrations.[70] Broad peaks observed around 3000–3300 $cm^{-1}$ are the peaks of N–H groups located at the edges of the heptazine units, which were also confirmed by XPS analysis later.[71] A peak around 2200 $cm^{-1}$ is barely seen and is attributed to the C≡N bond formed during the synthesis process, so that the defective structure begins to exhibit C≡N functionalities.[72] X-ray photoelectron spectroscopy (XPS) was conducted for oxidation state and chemical environment analysis of elements before and after the annealing process. The survey spectra (Fig. S3) showed that the materials are solely formed by carbon and nitrogen without any impurities. High-resolution XPS analysis of the C 1s and N 1s regions (Fig. 1d, e and Fig. S4) revealed similar spectral trends for both CN(X) and Nv-CN(X)-TG derivatives. In the C 1s spectra, peaks

 

at 284.5 eV, 285.7 eV, and 287.9 eV correspond to reference carbon (C–C, C=C), the C–N adjacent to the bridging amino group, and C=N bonds of tri-*s*-triazine units, respectively.[73] Furthermore, a shift of the C=N peak to higher binding energies in the annealed materials suggests that the formation of Nv alters the carbon atoms to become more electron-deficient. On the other hand, in the N 1s spectra, peaks observed at 398.4 eV, 399.7 eV, and 400.9 eV are attributed to surrounding N=C bonds outside of tri-*s*-triazine units, the central N–$(C)_3$ nitrogen atom in the ring, and bridging –$NH_x$ species, respectively.[73] Indeed, a decrease in the intensity of the N=C peak underlines the formation of Nv. Conversely, a slight increase in the peak area (Table S1) corresponding to –$NH_x$ species was observed, so that vacancy formation favors the enrichment of –$NH_x$ functionalities on the surface.[74] As the annealing temperature increased, the ratio of N=C to –$NH_x$ groups on the surface decreased, which was quantitatively determined by peak areas, which further supports that higher annealing temperatures result in a greater degree of defect formation within the structure.

To further investigate the structural changes in Nv-CN(C)-650Ar, solid-state $^{13}C$ cross-polarization magic angle spinning nuclear magnetic resonance (CP MAS NMR) spectroscopy was employed as shown in Fig. 1f. In the spectrum of pristine CN (C), characteristic signals at 156.2 and 164.1 ppm were attributed to $CN_2(NH_2)$ (C1) and $CN_3$ (C2) units of the CN framework, respectively. These aromatic carbon environments exhibit distinct chemical shifts due to variations in their proximity and orientation relative to edge hydrogen atoms, which influence shielding effects. In the case of Nv-CN(C)-650Ar, the intensity of the C2 peak increased compared to CN(C), suggesting that thermal treatment promoted the formation of additional hydrogen bonds within the tri-*s*-triazine units. Furthermore, the C1 signal shifted upfield, likely due to the disruption of π-electron delocalization caused by Nv. In contrast, the downfield shift of the C2 peak indicates the presence of electron-withdrawing groups introduced near these sites in the modified structure. Electron paramagnetic resonance (EPR) spectroscopy was employed to confirm the presence of Nv in CN(X) and Nv-CN(X)-TG samples and to evaluate their relative abundance, as shown in Fig. 1g. All samples exhibited a characteristic signal at $g$ = 2.0029, which is attributed to unpaired electrons localized in the π-conjugated tri-*s*-triazine units.[75] Furthermore, the EPR signal intensity followed the order: Nv-CN(C)-650Ar > Nv-CN(M)-650Ar > Nv-CN(D)-600$N_2$ > CN(M) > CN(C) > CN(D), indicating that the Nv concentration can be effectively tuned by varying the precursor type and annealing conditions. Elemental CHN analysis was performed to assess the overall chemical composition (C, N, and H) of the CN(X) and Nv-CN(X)-TG samples. As can be concluded by Table S2, higher annealing temperatures result in a lower N/C ratio, regardless of whether $N_2$ or Ar was used as an annealing atmosphere. Notably, the Nv-CN(C)-650Ar sample showed the lowest nitrogen content, which is attributed to the formation of Nv and the thermal decomposition of nitrogen-rich moieties during high-temperature annealing. These chemical changes overall in the nitrogen environment of heptazine units contribute to mid-gap states formation that was later evidenced by photophysical analyses (*vide infra*).

To investigate the morphological and topological characteristics of the synthesized materials, transmission electron microscopy (TEM) and scanning electron microscopy (SEM) analyses were conducted (Fig. 2 and Fig. S5). As shown in Fig. 2a and b, pristine CN(C), synthesized *via* thermal condensation of cyanamide, exhibits a layered and porous structure. Meanwhile, the TEM images of Nv-CN(C)-650Ar (Fig. 2c and d) reveal a thinner 2D architecture with more uniformly distributed and well-defined pores. Similarly, SEM images reveal that pristine CN(C) materials (Fig. 2e and f) exhibit a typical layered morphology, whereas Nv-CN(C)-650Ar (Fig. 2g and h) consist of thinner nanosheets with mesoporous nanostructure compared to other CN(X) and Nv-CN(X)-TG (Fig. S5). To gain further insight into the porous structure, nitrogen adsorption–desorption isotherms were measured to evaluate the Brunauer–Emmett–Teller (BET) surface areas of CN(X) and Nv-CN(X)-TG samples (Fig. S6). The introduction of Nv led to a notable increase in surface area, indicating enhanced porosity as shown in Fig. S6. All samples exhibited type IV isotherms with H1-type hysteresis loops, characteristic of mesoporous materials with uniform pore size distributions. These porous features are indicative of nitrogen-containing species release during post-annealing and play a crucial role in enhancing photocatalytic performance by increasing the number of active sites, expanding the specific surface area, and introducing structural defects that facilitate improved charge carrier mobility.

The Nv-engineering by thermal annealing is expected to have a substantial impact on the electronic structure and charge carrier dynamics of the material.[76] As discussed previously, these defects can introduce localized energy states and modified band edge positions. The following photophysical characterizations were performed to comprehensively evaluate these effects. Ultraviolet–visible diffuse reflectance spectroscopy (UV-Vis DRS) was employed to examine the photophysical properties of pristine CN(X) and Nv-CN(X)-TG derivatives. Compared to pristine CN(X) derivatives as shown in Fig. 3a and Fig. S7, Nv-CN(X)-TG derivatives exhibited a significant red shift in the absorption band edge to higher wavelengths up to 600 nm. A significant red shift in absorption edge is observed in Nv-CN(X)-650G samples as the annealing temperature increased up to 650 °C (Fig. S7). The shifts in absorption edges indicate enhanced light-harvesting capability for the Nv-CN(X)-TG derivatives, with Nv-CN(C)-650Ar exhibiting the most pronounced improvement among the annealed samples.[77] Furthermore, mid-gap states, located between the conduction band (CB) and valence band (VB), were observed,[78] which can be attributed to defect formation in the CN structure, contributing to sub-bandgap absorption. Tauc plots were constructed to estimate the optical bandgaps of CN(X) and Nv-CN(X)-TG derivatives (Fig. 3b and Fig. S8). The bandgap of pristine CN(X) derivatives was determined to be 2.7 eV, which is consistent with the reported literature values.[79] The decrease

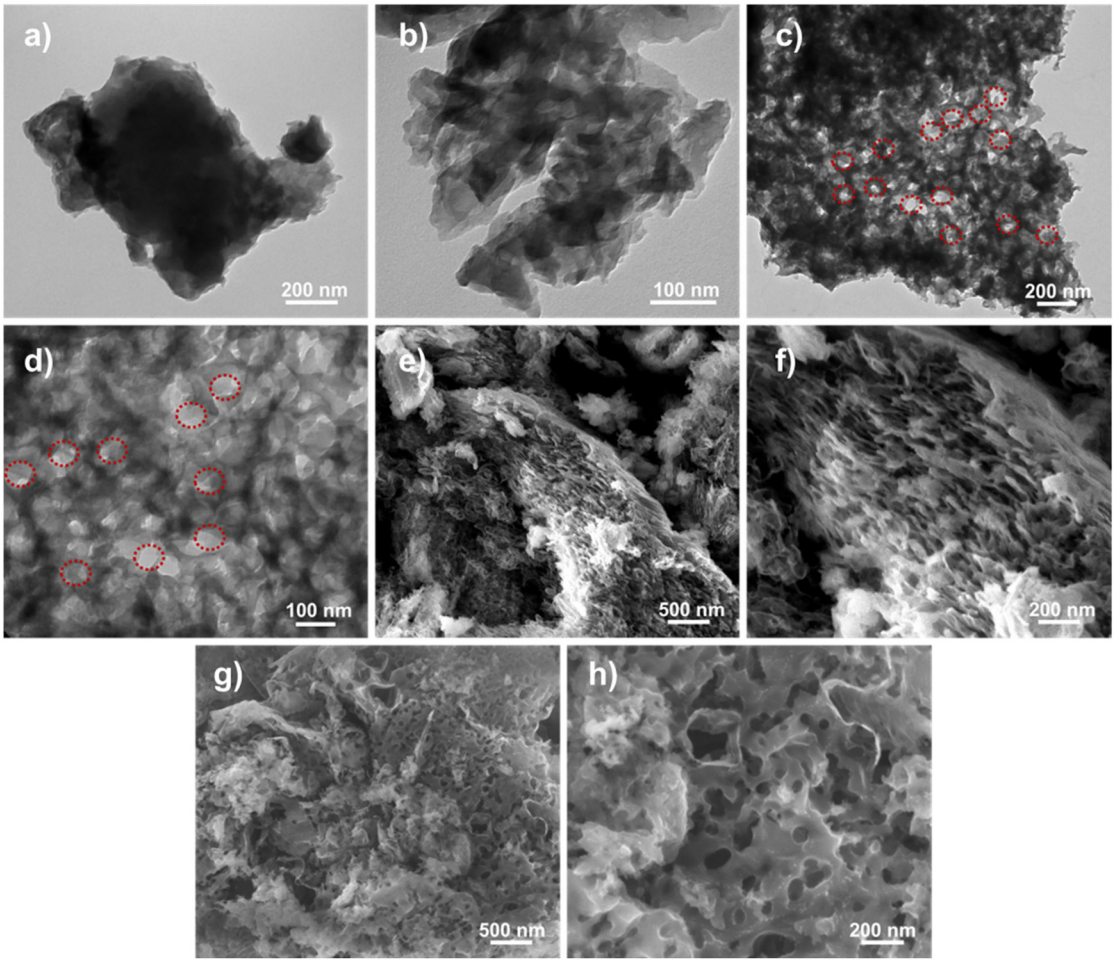


**Fig. 2** TEM images of (a and b) CN(C) and (c and d) Nv-CN(C)-650Ar, SEM images of (e and f) CN(C) and (g and h) Nv-CN(C)-650Ar.

in bandgap values down to 2.4–2.5 eV with the formation of Nv as the annealing temperature increases highlights the role of defect engineering in modifying photophysical properties.[80] The bandgap values corresponding to crafted mid-gap states are determined as 2.06 eV.[78,81] Moreover, samples synthesized under nitrogen atmosphere mostly exhibited higher bandgap values compared to their Ar-treated analogs (Fig. S8).[82] The variation in bandgap values suggests that annealing under distinct gas flow leads to a different defect formation mechanism. Photoluminescence (PL) spectroscopy was conducted to investigate the radiative charge recombination/separation behavior and kinetics of photogenerated electron–hole pairs in as-prepared materials. All samples exhibited a broad emission band centered between 450–520 nm upon excitation at 320 nm (Fig. 3c and Fig. S9). The emission peak wavelength of 460 nm for CN(X) samples corresponds to a characteristic energy of the $\pi$–$\pi^*$ transitions and band-to-band recombination processes in the CN structure.[83] Compared to their pristine structure, the Nv-CN(X)-TG samples demonstrated significantly diminished PL intensities, and the most pronounced diminishment was observed in the Nv-CN(C)-650Ar material. The decrease in emission intensity shows that the recombination is suppressed so that a more efficient separation of photogenerated charge carriers is achieved, especially in the vacancy-rich materials.[84] The charge carrier dynamics are further investigated by time-resolved photoluminescence (TRPL) measurements. The TRPL decay profiles of CN(X) and Nv-CN(X)-TG samples were fitted using an acknowledged biexponential function as a function of $\tau_1$ and $\tau_2$, the lifetimes of fast and slow decay components, respectively.[85] The fast component ($\tau_1$) is typically associated with surface recombination or mid-gap intervened processes, and the slow component ($\tau_2$) reflects the bulk recombination of charge carriers.[86] Fig. 3d illustrates that $\tau_{ave}$ of CN(C) decreased remarkably from 7.2 ns to 5.5 ns after annealing under argon at 650 °C. While CN(C) was fitted for $\tau_1$ and $\tau_2$, having 2.2 ns and 10.2 ns with 37.3% and 62.7% intensities, respectively, Nv-CN(C)-650Ar was fitted for $\tau_1$ and $\tau_2$, having 1.7 ns and 8.2 ns with 41.2% and 58.8% intensities, respectively. The decrease in the lifetime and the increase in the intensity of the fast component confirm the nitrogen vacancies promoting the nonradiative decay pathways and a more efficient separation through suppressed radiative recombination.[87] In contrast, the $\tau_{ave}$ of CN(D) and CN(M) increased after annealing, which suggests that the defect formation in these materials

 

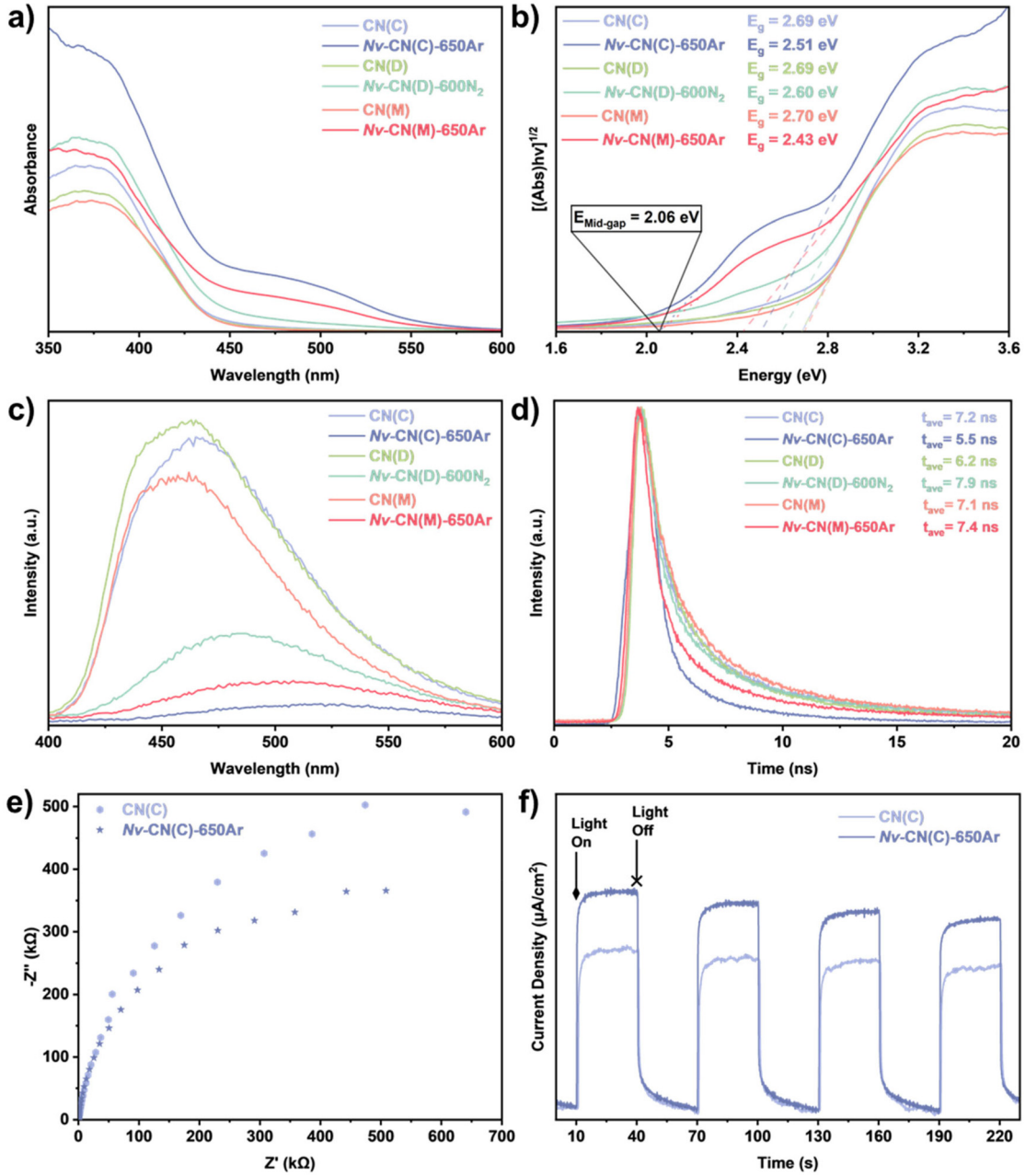


**Fig. 3** Photophysical characterization was given by (a) UV-Vis absorption spectra, (b) Tauc plots, (c) PL and (d) TRPL spectra of CN(X) derivatives and their most catalytically efficient Nv-CN(X)-TG derivatives, (e) Nyquist plots and (f) TPC responses of the most promising Nv-CN(C)-650Ar and pristine CN(C).

contributed more to carrier stabilization than mid-gap assisted recombination.[55]

From both PL and TRPL analyses, Nv-CN(C)-650Ar promises a remarkably higher photocatalytic activity than other materials synthesized along. Electrochemical impedance spectroscopy (EIS) measurements were carried out to assess the charge transfer behavior of CN(C) and Nv-CN(C)-650Ar. In Fig. 3e, the Nyquist plots for both samples exhibit a typical semicircular arc in the high-frequency region that represents the interfacial charge transfer resistance at the electrode–electrolyte interface.[88] Nv-CN(C)-650Ar displays a significantly smaller arc radius compared to pristine CN(C), and so a more efficient charge transport. The reduction in charge transfer resistance can be attributed to the introduction of Nv during the annealing process. In order to assess the photo-responsive behavior and interfacial charge transfer efficiency of CN(C) and its annealed derivative Nv-CN(C)-650Ar, transient photocurrent (TPC) measurements were performed under dark and visible-light illumination. As illustrated in Fig. 3f, both materials exhibit a drastic increase in photocurrent density upon

illumination, revealing their fundamental photoactivity. Expectedly, Nv-CN(C)-650Ar generated a significantly higher and more stable photocurrent density compared to pristine CN(C), so that a more efficient generation, separation, and transport of photogenerated charge carriers were achieved. Altogether, these results collectively confirm that defect engineering not only alters the structural properties of CN but also enhances charge separation and transport dynamics. The synergy of these effects suggests that annealed materials, specifically Nv-CN(C)-650Ar, are the most promising candidates for the superior photocatalytic activity.

### Utilization of the Nv-CNs in C–P bond formation

Combining all these structural, photophysical, and electrochemical characterizations, Nv-rich materials, especially Nv-CN(C)-650Ar, are anticipated to predominate over their pristine derivatives in visible-light-driven photoredox C–P bond formation. To evaluate the photocatalytic activity of as-synthesized Nv-CN-based materials, a model C–P bond-forming reaction was designed using *N*-(4-acetylphenyl)-tetrahydroisoquinoline (**1**) and 9,10-dihydro-9-oxa-10-phosphaphenanthrene-10-oxide (DOPO, **2**) as substrates. Compound **1** is a tertiary amine bearing an electron-withdrawing acetyl group at its N-functionality that was intentionally selected for the model reaction. Considering the reported oxidation potentials of the tetrahydroisoquinoline derivatives ($E_{ox}$ = (+1.07 V) − (+2.38 V) *vs.* SCE in MeCN), compound **1** has a relatively medium level challenging potential with its deactivated α-C($sp^3$)–H site.[31,89] Compound **2** is a phosphine oxide heterocycle that served as the organophosphorus source. The model reaction (Fig. 4a) was performed in oxygenated MeCN using a photoreactor system with tunable-wavelength LEDs, active cooling *via* a fan and chiller, and operated under controlled-intensity blue light irradiation. At first, all synthesized materials (3 mg each) were

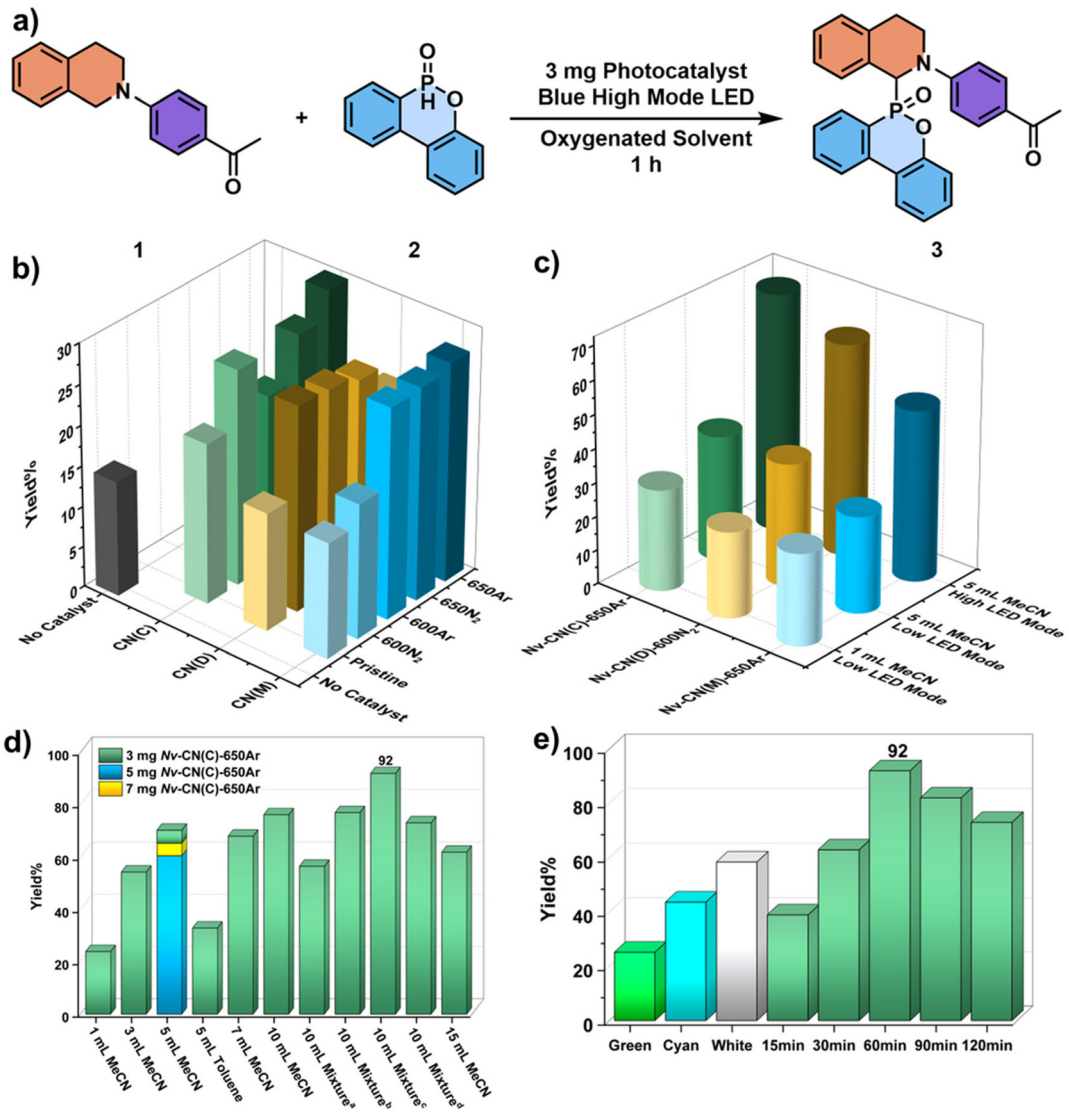


**Fig. 4** (a) The model reaction. The optimizations of (b) catalyst type, (c) light intensity, (d) solvent screening [a]MeCN/DMF (9 : 1), [b]MeCN/THF (9 : 1), [c]MeCN/DMSO (9 : 1), [d]MeCN/DMSO (9.5 : 0.5), (e) irradiation color and duration.

tested under identical conditions, which are 1 mL MeCN (saturated with $O_2$), blue LED (low mode), and 1 hour irradiation. Nv-engineered materials consistently outperformed their pristine catalysts in photocatalytic yield, and Nv-CN(C)-650Ar, Nv-CN(D)-600$N_2$, and Nv-CN(M)-650Ar showed the highest yields among the cyanamide, dicyandiamide, and melamine-derived series, respectively (Fig. 4b, for details, see Table S3). While the reaction yielded 14% in the absence of any catalysts, the photocatalysts produced yields in the range of 15–30% so that the results were promising, but there was a need for optimization. Since Nv-CN(X)TG is a polymeric material, poor dispersion in low solvent volumes was suspected to hinder catalytic efficiency. Increasing the solvent volume to 5 mL MeCN led to an improvement in yield of up to 37%, with Nv-CN(C)-650Ar having the highest yield (Fig. 4c). Subsequently, the intensity of light irradiation was increased by switching the LED to high mode, which resulted in a sharp increase in yield to 70% under identical conditions. Conversely, increasing the catalyst loading to 5 mg and 7 mg led to diminished yields, most likely due to excessive light scattering at higher particle concentrations, and so 3 mg of photocatalyst was used as the optimal catalyst amount in subsequent experiments (Fig. 4d). Solvent volume and ratio were further optimized, and MeCN volumes up to 15 mL were tested, with the highest yield (76%) achieved at 10 mL of volume. Solvent mixtures were then explored while maintaining a constant total volume of 10 mL. Among the mixtures tested, MeCN/DMSO (9 : 1) provided the highest yield of 92%. In a time-course study ranging from 15 min to 2 h, the product yield increased up to 1 h, after which a gradual decline was observed upon prolonged reaction times (Fig. 4e). To understand this behavior, the reaction mixture obtained at extended irradiation times was analyzed by $^1$H NMR and GC-MS and compared with the spectra of pure compound **3**. These analyses revealed the formation of additional byproducts, consistent with oxidative degradation of substrate **1**. Initially, the decreased yield was tentatively attributed to possible phosphorus adsorption or deactivation of the photocatalyst. However, ICP-MS analysis of the recovered catalyst showed no detectable phosphorus uptake. We therefore attribute the decline in yield at longer reaction times to product degradation and over-oxidation of the reactants under prolonged photochemical conditions (Fig. S10 and S11). After all these findings, the optimized conditions are defined as 3 mg Nv-CN(C)-650Ar in 10 mL MeCN/DMSO (9 : 1) and under blue LED (high mode, 457 nm) irradiation for 1 hour (for detail, see Table S3). Finally, the influence of light energy was investigated by varying the wavelength. As expected, a decrease in yield was observed with lower-energy light sources that were tried with white (correlated color temperature of 6500 K), cyan (500 nm), and green (523 nm), since the energy of photons is reduced as the wavelength increases. Moreover, the dark control experiment further confirmed the photocatalytic nature of the reaction, resulting in no observable product formation. The reaction conducted under white LED for 1 hour gave a yield (59%) comparable to that obtained under blue LED in only 30 minutes (63%). Overall, the photocatalyst developed *via* defect engineering achieved an impressive yield of 92%, notably surpassing conventional metal-catalyzed systems with comparable substrates.[90] The optimized conditions yield a diastereomeric ratio of 1 : 3 that is marginally below the reported values of phosphorylation reactions with metal catalysis in the literature.[91,92] This remarkable enhancement underscores the pivotal role of Nv in promoting efficient charge separation and boosting photocatalytic performance under mild, metal-free conditions, as evidenced by our characterization results.

### The band diagram, mechanistic studies, and reusability test

In order to gain a deeper insight into the photocatalytic performance of as-synthesized materials, the CB and VB edge positions were determined by Mott–Schottky analysis and XPS-VB spectroscopy, respectively. The flat band potentials ($E_{fb}$) of the pristine CN(X) and Nv-CN(X)-TG materials were first found using Mott–Schottky analysis (Fig. 5a, c and e).

In the CN(C) series, the $E_{fb}$ of pristine CN(C) was measured as −0.88 V *vs.* $Hg/Hg_2Cl_2$, which shifted to −0.80 V in Nv-CN(C)-650Ar, indicating a change in electronic structure upon Nv formation. These potential values were converted to the normal hydrogen electrode (NHE) scale using the relation: ($E_{fb}$ (*vs.* NHE) = $E_{fb}$ (*vs.* $Hg/Hg_2Cl_2$) + 0.24 V).[93] Accordingly, the $E_{fb}$ values *vs.* NHE were calculated to be −0.64 V for CN(C) and −0.56 V for Nv-CN(C)-650Ar. The positive slopes observed in the Mott–Schottky plots confirm the n-type semiconductor behavior of all CN-based materials.[49] In such semiconductors, the Fermi level ($E_F$) is typically approximated by the $E_{fb}$. Since the CB edge lies approximately 0.10–0.20 V more negative than $E_F$,[94] the CB potentials for CN(C) and Nv-CN(C)-650Ar were estimated to be −0.74 V and −0.66 V *vs.* NHE, respectively. Similar calculations were performed for dicyandiamide and melamine-based materials. The VB potentials (Fig. 5b, d and f) of annealed Nv-CN(X)-TG materials were measured as 1.64–1.79 eV using the VB-XPS spectrum, while the pristine materials were found as 1.82–1.85 eV. The potential of the VB converted by the equation of ($E_{NHE} = \varphi + E_{VB\text{-}XPS} - 4.44$, where $E_{NHE}$: normal hydrogen electrode; $\varphi$: electron work function of the XPS analyzer that is 4.543; $E_{VB\text{-}XPS}$: VB value was tested by VB-XPS),[95,96] the VB edge potentials of pristine and Nv-CN(X)-TG materials were found to be 1.92–1.95 eV and 1.74–1.89 eV, respectively. An overall schematic representation of the band edge positions for all materials was presented in Fig. 5g.

After investigation of band positions, mechanistic studies were conducted to further understand the underlying photocatalytic pathway. Radical scavenger experiments were conducted to identify the key reactive species involved in the C–P bond formation reaction under visible-light irradiation. The scavenger experiments (Fig. 6a) were performed with p-benzoquinone (BQ), 2,2,6,6-tetramethylpiperidine-1-oxyl (TEMPO), triethanolamine (TEOA), isopropanol (IPA), and silver nitrate ($AgNO_3$) scavengers. The BQ scavenger is used for superoxide radical anions ($^{\bullet}O_2^-$) that resulted in a yield drop to 50% which suggests that superoxide species have a partial contribution to the C–P bond formation.[97] The addition of TEMPO,

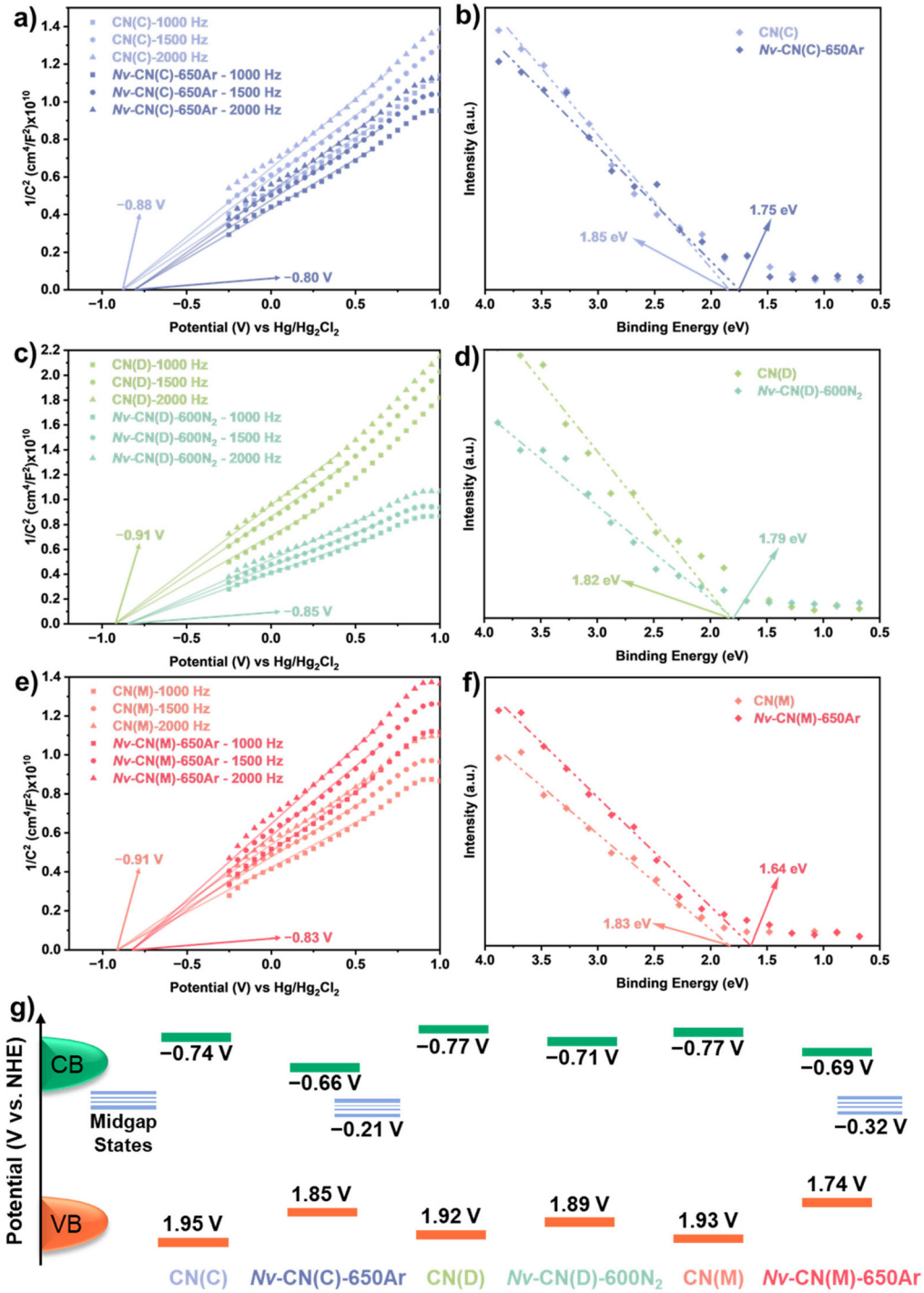


**Fig. 5** Mott–Schottky plots of pristine and annealed CN derivatives with precursors of (a) cyanamide, (b) dicyandiamide, and (c) melamine at 1000, 1500, and 2000 Hz. XPS-VB spectra for pristine and annealed CN derivatives with precursors of (d) cyanamide, (e) dicyandiamide, and (f) melamine, (g) the band structure for pristine CN(X) and Nv-CN(X)-TG derivatives.

a scavenger for free radicals, completely suppressed the reaction so that a radical cation intermediate was generated probably through single-electron oxidation of compound **1**.[98] Similarly, TEOA is a hole scavenger and dramatically reduced the yield to 7% which underlines the critical role of photo-induced holes for initiation of the oxidation.[99] IPA and sodium azide ($NaN_3$) are hydroxyl radical ($^{\bullet}OH$) and singlet oxygen ($^1O_2$) scavengers, respectively, causing a moderate reduction in yield to 61–64% implying that neither hydroxyl radicals nor singlet oxygen are the main species of the reaction but they may play a secondary or supporting role.[100] Furthermore, the presence of $AgNO_3$, a potent electron scaven-

 

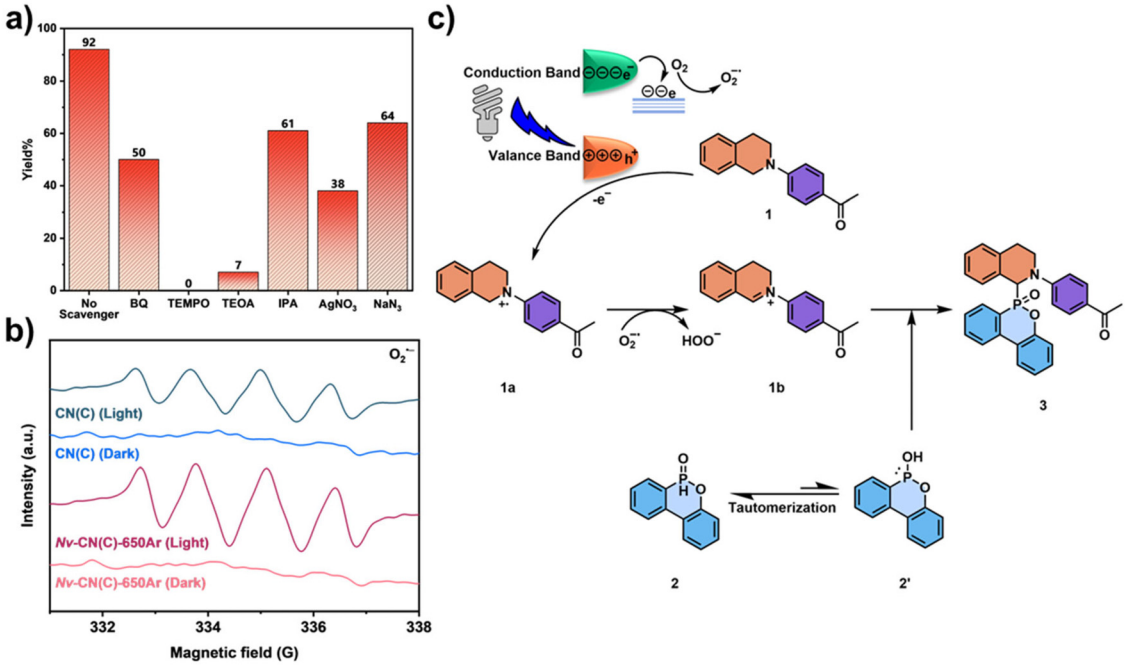


**Fig. 6** (a) The scavenger experiments, (b) the light-on/off EPR spectra of pristine CN(C) and Nv-CN(C)-650Ar for superoxide radical anion and (c) the proposed reaction mechanism.

ger, resulted in a yield decrease to 38% which confirms the importance of photogenerated electrons during the catalytic cycle.[101] To demonstrate the influence of Nv on the formation of reactive oxygen species under irradiation, light-on EPR spectroscopy (Fig. 6b) was employed using DMPO as a spin-trapping agent for superoxide radical anions ($O_2^{\bullet-}$). Upon visible-light illumination, both pristine CN(C) and Nv-CN(C)-650Ar exhibited the characteristic signal pattern. However, the Nv-material consistently produced substantially higher signal intensity that underlines enhanced $O_2^{\bullet-}$ generation under identical conditions. From the scavenger experiments and EPR results, a plausible mechanism was proposed in Fig. 6c as similar to the previous reports.[31,102] After the formation of photogenerated charge carriers under light illumination, the process begins with a simultaneous single-electron transfer (SET): an electron from the CB is transferred to molecular oxygen, generating a superoxide anion radical ($E_{red}(O_2/O_2^{\bullet-})$ = −0.33 V *vs.* NHE),[93] while a hole in the VB accepts an electron from compound **1**, forming the radical cation intermediate **1a**. Intermediate **1a** was then converted into an iminium cation **1b** through a hydrogen-atom transfer (HAT) by superoxide anion radicals.[89] Synchronously, compound **2** tautomerizes to compound **2′**, which is a nucleophile due to a lone pair on phosphorus.[103] Compound **2′** attacks the electrophilic α-carbon of the iminium cation to form the desired product **3**.

To assess the practical applicability, the stability and reusability of Nv-CN(C)-650Ar were tested by subjecting the photocatalyst to ten consecutive photocatalytic cycles under the optimized reaction conditions. As shown in Fig. S12a, the yield remained relatively high with a minute decline over the first three cycles, and the initial durability of the photocatalyst was fine. However, a gradual decrease in activity was observed in subsequent runs as the yields dropped to 79% in the fourth and 71% in the fifth cycle. While yields remained around 50% between sixth and ninth cycles, the yield diminishes at the tenth cycle due to a reduction in the catalyst amount. Nevertheless, the heterogeneous photocatalyst retained over 70% yield after five cycles and is reusable for practical applications in visible-light-driven C–P bond formations. Post-characterization of Nv-CN(C)-650Ar using XRD, FTIR and XPS analyses were employed in Fig. S12b–f to compare structural integrity of the photocatalyst before and after use. All these analyses, especially the high-resolution XPS N 1s spectrum, revealed alterations in the peaks attributed to Nv, and the XRD pattern further confirmed the presence of a small amount of impurity in the crystal structure. Furthermore, TEM analysis revealed that both the thickness and porous nature of the catalysts changed compared to its fresh version, as shown in Fig. S13a–d. The observed increase in layer thickness and structural alterations indicates a partial healing of nitrogen vacancies, which is associated with a decline in photocatalytic activity.

### The substrate scope of Nv-CN(C)-650Ar catalyzed C($sp^3$)–P bond formation

To explore the generality of the developed photocatalyst, a series of structurally diverse tertiary amines and organophosphorus compounds were mostly subjected to the optimized reaction conditions using Nv-CN(C)-650Ar as the photocatalyst (Fig. 7). The scope was initially expanded to include different

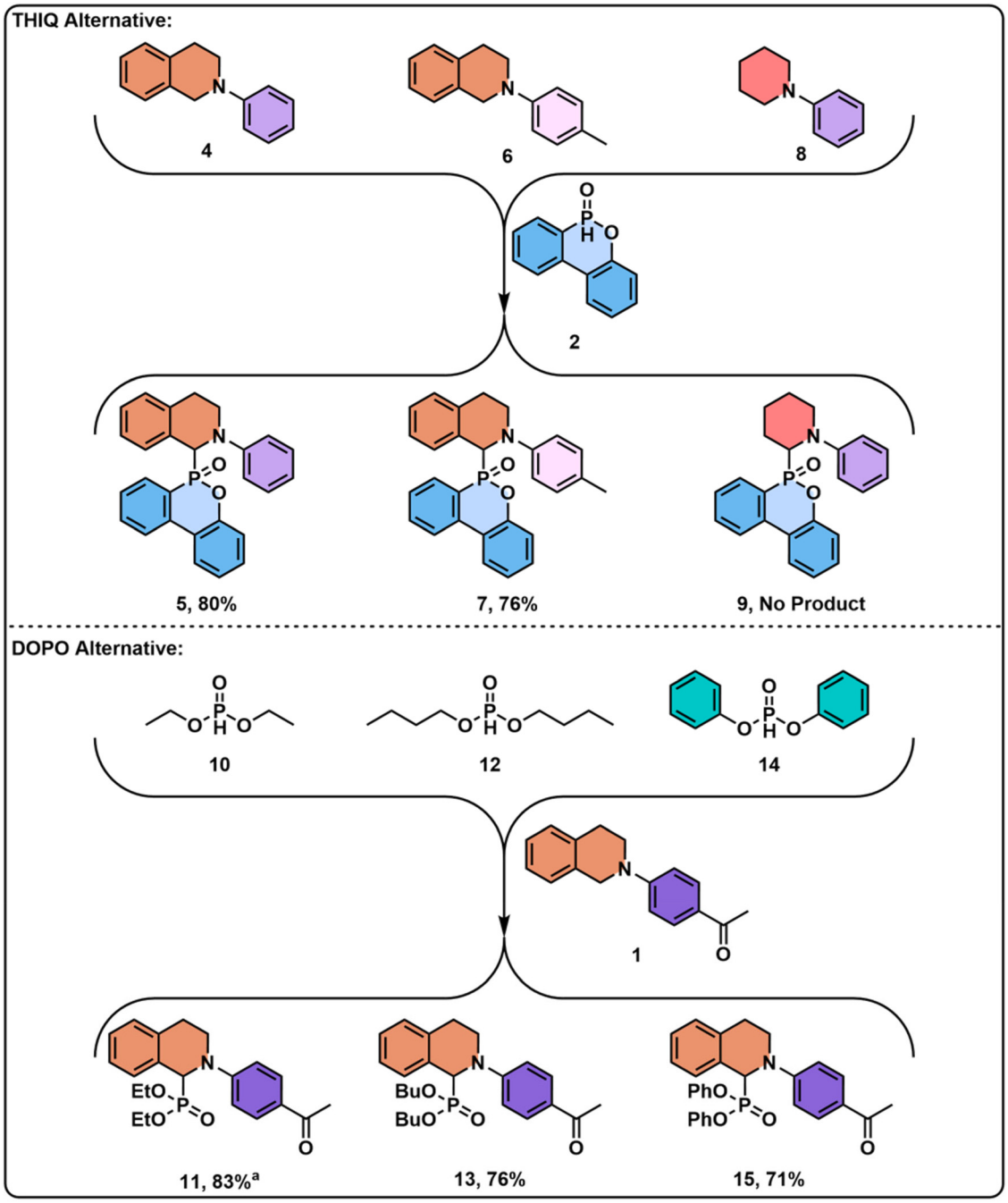


Fig. 7 The substrate scope of the developed photocatalyst. [a]In 5 mL MeCN, 5 h reaction time.

C($sp^3$)–H coupling partners with P(O)H compounds under standard conditions. The reaction showed broad functional group tolerance on the phenyl ring, including unsubstituted **4** and methyl-substituted **6** derivatives, reflecting a range of electronic effects. Notably, *N*-substituted tetrahydroisoquinoline derivatives provided high yields of 80% for compound **4** and 76% for compound **6**, respectively, due to their electron-rich nature. In contrast, *N*-substituted piperidine showed no reactivity, likely due to the low activity of its α-C($sp^3$)–H bond.[104] Further exploration with different phosphoesters and compound **1** under the same conditions revealed that diethyl, dibutyl, and diphenyl phosphonates were also effective, delivering the desired products in yields of 83% (**11**), 76% (**13**), and 71% (**15**), respectively. These results correlated with the steric bulk of the phosphoesters.[18]

The yields for the substrates were approximately between 70–80%, which were competitive with those in the literature reactions performed with metal-catalysis.[105,106] These substrate trials confirm that the developed photocatalyst is not only efficient for the model reaction but also adaptable to a

 

broader range of substrates. Nv-CN materials, specifically Nv-CN(C)-650Ar, have a superior potential for their utility in the construction of C–P bonds under mild and sustainable conditions.

In this work, a sustainable and chemoselective approach for C($sp^3$)–P bond formation through Nv-CN photocatalyst having a versatile and green synthesis was demonstrated. The reaction between tetrahydroisoquinoline derivatives and phosphoesters was generalized using similar substrates. Nevertheless, the optimized conditions fail to perform phosphorylation of other types of substrates including diazonium salts and some other heteroaromatic compounds. Since this work establishes a green strategy for such synthesis, the future work in this area would focus on the broadening of the usability of the protocol in various substrates while preserving sustainability. Furthermore, the stereoselectivity of the reaction would be improved more to reach reported diastereomeric ratio values obtained by metal-catalysis in the literature.

## Conclusions

In summary, this study provides a comprehensive investigation into the design and application of Nv-CN materials, synthesized *via* thermal annealing of three nitrogen-rich precursors under systematically varied conditions for photoredox C($sp^3$)–P bond formation. Among the synthesized twelve photocatalysts, Nv-CN(C)-650Ar efficiently fostered the photooxidative C($sp^3$)–P bond formation under mild conditions and achieved up to 92% yield in 1 hour without requiring metals or toxic oxidants. The superior photocatalytic performance of Nv-CN(C)-650Ar, compared to CN(X) and other Nv-CN(X)-TG materials, is attributed to its optimized structural, morphological, and photophysical properties. XRD analysis revealed that the (002) diffraction peak of Nv-CN(C)-650Ar is the broadest among all samples, indicating a thinner, more disordered, and amorphous layered structure. XPS and CHN elemental analyses confirmed the formation of more $NH_x$ surface groups and a lower nitrogen-to-carbon stoichiometry, reflecting a higher concentration of nitrogen vacancies. These findings were further supported by EPR spectroscopy, which showed the highest signal intensity, indicating the greatest defect density. SEM and BET surface area measurements demonstrated that Nv-CN(C)-650Ar possesses a more porous morphology and the largest surface area, enhancing the accessibility of active sites. Additionally, UV–DRS revealed stronger visible-light absorption with mid-gap state, and based on Tauc plot analysis, a narrower bandgap compared to other samples. PL and TRPL analyses exhibited significantly reduced emission intensity and shorter carrier lifetimes, indicating suppressed charge recombination and more efficient charge separation. These combined features collectively account for the enhanced photocatalytic activity of Nv-CN(C)-650Ar in the photoredox C($sp^3$)–P bond formation. The substrate scope was successfully expanded to a variety of challenging organophosphorus compounds, highlighting the versatility and functional group tolerance of the catalyst system. Mechanistic studies, including radical scavenger experiments, indicated that the reaction proceeded *via* a single-electron oxidation pathway initiated by photogenerated holes and mediated by superoxide radicals. In addition, reusability tests demonstrated excellent stability and recyclability of Nv-CN(C)-650Ar over five consecutive cycles without any notable loss in activity. This metal-free strategy enables the sustainable synthesis of P(v)-based organophosphorus compounds, widely demanded in pharmaceuticals, bioactive agents, and flame retardants. Overall, this work not only deepens the mechanistic understanding of defect engineering in CN-based photocatalysts but also paves the way for their broader application in selective and green organic transformations.

## Author contributions

B. B. did formal analysis, methodology, validation, investigation, writing original draft, and visualization. M. S. O. did conceptualization, formal analysis, methodology, validation, investigation, writing original draft, supervision, project administration, and visualization. K. S. did formal analysis and investigation. H. L. J. did writing review and editing, supervision, and funding acquisition. Z. E. did conceptualization, formal analysis, methodology, validation, investigation, supervision, project administration, writing original draft, and visualization. O. M. did conceptualization, writing review and editing, supervision, funding acquisition, project administration, and validation.

## Conflicts of interest

The authors declare that they have no known competing financial interests or personal relationships that could have appeared to influence the work reported in this paper.

## Data availability

The data supporting this article have been included as part of the supplementary information (SI). Supplementary information: abbreviations, characterization of catalysts, materials, and products (NMR). See DOI: https://doi.org/10.1039/d5gc06242j.

## Acknowledgements

Ö. M. thanks the Turkish Academy of Sciences (TÜBA) for the financial support. B. B. thanks the Scientific and Technological Research Council of Türkiye (TÜBİTAK) for the 2209A undergraduate research project. H. L. J. thanks International Partnership Program of CAS (123GJHZ2022028MI) and National Natural Science Foundation of China (W2512006). All authors thank Mert Efe

Özlüdemir for graphical abstract design. The authors thank Osman Nuri ASLAN and Eastern Anatolia High Technology Application and Research Center (DAYTAM) for assistance with the ICP-MS analysis.

## References

1 J. H. Docherty, T. M. Lister, G. Mcarthur, M. T. Findlay, P. Domingo-Legarda, J. Kenyon, S. Choudhary and I. Larrosa, *Chem. Rev.*, 2023, **123**, 7692–7760.
2 J. Liu, R. Liang, Q. Yan, L. Zheng, Z.-Q. Liu and S. Pu, *Org. Chem. Front.*, 2025, **12**, 3065–3106.
3 R. N. Ghoghari and K. H. Chikhalia, *J. Organomet. Chem.*, 2025, **1027**, 123512.
4 Y. Liu, X. Li and J. Li, *Tetrahedron*, 2024, **166**, 134234.
5 M. S. Özer and S. Gaan, *Prog. Org. Coat.*, 2022, **171**, 107027.
6 S. C. Fields, *Tetrahedron report number 506 Synthesis of Natural Products Containing a C-P Bond*, 1999, vol. 55.
7 W. Tang and X. Zhang, *Chem. Rev.*, 2003, **103**, 3029–3069.
8 S. Dong, Y. Wang, L. Liu, H. Jia, Y. Zang, L. Zu, T. Lan and J. Wang, *ACS Omega*, 2023, **8**, 48825–48842.
9 N. K. Mishra, J. Park, H. Oh, S. H. Han and I. S. Kim, *Tetrahedron*, 2018, **74**, 6769–6794.
10 S. Wendels, T. Chavez, M. Bonnet, K. Salmeia and S. Gaan, *Materials*, 2017, **10**, 784.
11 L. Ye, Q. Gan, X. Wang, X. Chen, X. Zhang, Y. Liu and Z. Jiang, *ACS Sustainable Chem. Eng.*, 2025, **13**, 10165–10174.
12 H. Li, Y. Liu and S. Kramer, *Angew. Chem. Int. Ed.*, 2025, **64**, e202420613.
13 B. Zheng, L. Xue, C. Dai, J. Liu and H. Cheng, *J. Org. Chem.*, 2022, **87**, 5287–5295.
14 A. Tanoue, W. J. Yoo and S. Kobayashi, *Adv. Synth. Catal.*, 2013, **355**, 269–273.
15 M. Rueping, J. Zoller, D. C. Fabry, K. Poscharny, R. M. Koenigs, T. E. Weirich and J. Mayer, *Chem. – Eur. J.*, 2012, **18**, 3478–3481.
16 D. Leca, L. Fensterbank, E. Lacôte and M. Malacria, *Chem. Soc. Rev.*, 2005, **34**, 858–865.
17 K. N. Yuan, T. Xie, J. B. Wang, D. Wang and M. Shang, *Angew. Chem. Int. Ed.*, 2025, **64**, e202500744.
18 Q. Fu, D. Yi, Z. Zhang, W. Liang, S. Chen, L. Yang, Q. Zhang, J. Ji and W. Wei, *Org. Chem. Front.*, 2017, **4**, 1385–1389.
19 P. Y. Geant, J. P. Uttaro, S. Peyrottes and C. Mathé, *Eur. J. Org. Chem.*, 2017, 3850–3855.
20 A. Batra and K. N. Singh, *Eur. J. Org. Chem.*, 2020, 6676–6703.
21 S. Mandal, T. Bera, G. Dubey, J. Saha and J. K. Laha, *ACS Catal.*, 2018, **8**, 5085–5144.
22 V. Vershinin and D. Pappo, *Org. Lett.*, 2020, **22**, 1941–1946.
23 H. Ueda, K. Yoshida and H. Tokuyama, *Org. Lett.*, 2014, **16**, 4194–4197.
24 A. E. Wendlandt, A. M. Suess and S. S. Stahl, *Angew. Chem. Int. Ed.*, 2011, **50**, 11062–11087.
25 L. Niu, S. Wang, J. Liu, H. Yi, X. A. Liang, T. Liu and A. Lei, *Chem. Commun.*, 2018, **54**, 1659–1662.
26 W. P. To, Y. Liu, T. C. Lau and C. M. Che, *Chem. – Eur. J.*, 2013, **19**, 5654–5664.
27 F. Gao, W. Xiao, S. Li and B. Yu, *ACS Appl. Mater. Interfaces*, 2022, **14**, 19278–19284.
28 G. Y. Kim, S. Park, G. Park, Y. Kang, H. Kim and J. Kim, *J. Org. Chem.*, 2025, **90**, 5966–5972.
29 B. Mu, L. Zhang, G. Lv, K. Chen, T. Wang, J. Chen, T. Huang, L. Guo, Z. Yang and Y. Wu, *J. Org. Chem.*, 2022, **87**, 10146–10157.
30 M. C. Mayorquín-Torres, A. Simoens, E. Bonneure and C. V. Stevens, *Chem. Rev.*, 2024, **124**, 7907–7975.
31 S. S. Zhu, Y. Liu, X. L. Chen, L. B. Qu and B. Yu, *ACS Catal.*, 2022, **12**, 126–134.
32 A. Modi, C. Gosmini and A. Auffrant, *Chem. – Asian J.*, 2025, **20**, e202401780.
33 C. M. Aitchison, S. Gonzalez-Carrero, S. Yao, M. Benkert, Z. Ding, N. P. Young, B. Willner, F. Moruzzi, Y. Lin, J. Tian, P. D. Nellist, J. R. Durrant and I. McCulloch, *Adv. Mater.*, 2024, **36**, 2300037.
34 C. Rosso, G. Filippini, A. Criado, M. Melchionna, P. Fornasiero and M. Prato, *ACS Nano*, 2021, **15**, 3621–3630.
35 A. Kocaarslan, Z. Eroglu, G. Yilmaz, O. Metin and Y. Yagci, *ACS Macro Lett.*, 2021, **10**, 679–683.
36 G. Zhang, Y. Xu, C. He, P. Zhang and H. Mi, *Appl. Catal., B*, 2021, **283**, 119636.
37 W.-J. Ong, L.-L. Tan, Y. H. Ng, S.-T. Yong and S.-P. Chai, *Chem. Rev.*, 2016, **116**, 7159–7329.
38 A. Thomas, A. Fischer, F. Goettmann, M. Antonietti, J. O. Müller, R. Schlögl and J. M. Carlsson, *J. Mater. Chem.*, 2008, **18**, 4893–4908.
39 T. O. Ajiboye, A. T. Kuvarega and D. C. Onwudiwe, *Nano-Struct. Nano-Objects*, 2020, **24**, 100577.
40 Y. Zhang, J. Liu, G. Wu and W. Chen, *Nanoscale*, 2012, **4**, 5300–5303.
41 X. Wang, S. Blechert and M. Antonietti, *ACS Catal.*, 2012, **2**, 1596–1606.
42 S. Cao, J. Low, J. Yu and M. Jaroniec, *Adv. Mater.*, 2015, **27**, 2150–2176.
43 J. Fu, J. Yu, C. Jiang and B. Cheng, *Adv. Energy Mater.*, 2018, **8**, 1701503.
44 X. Wu, F. Chen, X. Wang and H. Yu, *Appl. Surf. Sci.*, 2018, **427**, 645–653.
45 A. Durairaj, T. Sakthivel, S. Ramanathan and S. Vasanthkumar, *ACS Omega*, 2019, **4**, 6476–6485.
46 Y. Sun, V. Kumar and K.-H. Kim, *Sep. Purif. Technol.*, 2023, **305**, 122413.
47 C. Tang, M. Cheng, C. Lai, L. Li, X. Yang, L. Du, G. Zhang, G. Wang and L. Yang, *Coord. Chem. Rev.*, 2023, **474**, 214846.
48 G. Liao, C. Li, X. Li and B. Fang, *Cell Rep. Phys. Sci.*, 2021, **2**, 100355.

 

49 Z. Eroglu, M. S. Ozer and O. Metin, *ACS Sustainable Chem. Eng.*, 2023, **11**, 7560–7572.
50 M. Benedet, G. A. Rizzi, A. Gasparotto, N. Gauquelin, A. Orekhov, J. Verbeeck, C. Maccato and D. Barreca, *Appl. Surf. Sci.*, 2023, **618**, 156652.
51 T. Fidan, M. Torabfam, Q. Saleem, C. Wang, H. Kurt, M. Yüce, J. Tang and M. K. Bayazit, *Adv. Energy Sustainability Res.*, 2021, **2**, 2000073.
52 Q. Li, S. Zhao, B. Jiang, M. Jaroniec and L. Zhang, *Mater. Today*, 2024, **80**, 886–904.
53 J. Tan, N. Tian, Z. Li, J. Li, X. Yao, M. Vakili, Y. Lu and T. Zhang, *Chem. Eng. J.*, 2021, **421**, 127729.
54 A. Kumar, P. Raizada, A. Hosseini-Bandegharaei, V. K. Thakur, V.-H. Nguyen and P. Singh, *J. Mater. Chem. A*, 2021, **9**, 111–153.
55 Z. Eroglu, M. S. Ozer and Ö. Metin, *ChemCatChem*, 2024, **16**, e202301560.
56 Q. Lai, H. Zheng, Z. Tang, D. Bi, N. Chen, X. Liu, J. Zheng and Y. Liang, *ACS Appl. Mater. Interfaces*, 2021, **13**, 61129–61138.
57 B. Gao, M. Dou, J. Wang, S. Li, D. Wang, L. Ci and Y. Fu, *Chem. Eng. J.*, 2021, **426**, 131677.
58 X. Yu, S. Ng, L. K. Putri, L. Tan, A. R. Mohamed and W. Ong, *Small*, 2021, **17**, 2006851.
59 Y. Zhang, Z. Huang, C.-L. Dong, J. Shi, C. Cheng, X. Guan, S. Zong, B. Luo, Z. Cheng, D. Wei, Y. Huang, S. Shen and L. Guo, *Chem. Eng. J.*, 2022, **431**, 134101.
60 Q. Zhang, X. Chen, Z. Yang, T. Yu, L. Liu and J. Ye, *ACS Appl. Mater. Interfaces*, 2022, **14**, 3970–3979.
61 T. Roongcharoen, P. Mano, T. Jitwatanasirikul, P. Sikam, T. Butburee, K. Takahashi and S. Namuangruk, *Appl. Surf. Sci.*, 2022, **595**, 153527.
62 M. Jiang, M. Huang, J. Cong, Y. Yao, W. Sun and B. Wang, *J. Photochem. Photobiol., A*, 2024, **448**, 115324.
63 T. Kubanaliev, Z. Eroglu, M. S. Ozer and Ö. Metin, *Catal. Sci. Technol.*, 2023, **13**, 2317–2329.
64 G. Filippini, F. Longobardo, L. Forster, A. Criado, G. Di Carmine, L. Nasi, C. D'Agostino, M. Melchionna, P. Fornasiero and M. Prato, *Sci. Adv.*, 2020, **6**, 9923–9934.
65 R. Li and R. A. Sheldon, *Green Chem.*, 2017, **19**, 18–43.
66 O. Altan and Ö. Metin, *Appl. Surf. Sci.*, 2021, **535**, 147740.
67 S. Midya, A. Ali and D. P. Hari, *Nat. Commun.*, 2025, **16**, 6233.
68 Y. Zhang, S. Zong, C. Cheng, J. Shi, P. Guo, X. Guan, B. Luo, S. Shen and L. Guo, *Appl. Catal., B*, 2018, **233**, 80–87.
69 J. Liu, T. Zhang, Z. Wang, G. Dawson and W. Chen, *J. Mater. Chem.*, 2011, **21**, 14398–14401.
70 P. Praus, L. Svoboda, M. Ritz, I. Troppová, M. Šihor and K. Kočí, *Mater. Chem. Phys.*, 2017, **193**, 438–446.
71 A. B. Jorge, D. J. Martin, M. T. S. Dhanoa, A. S. Rahman, N. Makwana, J. Tang, A. Sella, F. Corà, S. Firth, J. A. Darr and P. F. McMillan, *J. Phys. Chem. C*, 2013, **117**, 7178–7185.
72 J. Liu, W. Fang, Z. Wei, Z. Qin, Z. Jiang and W. Shangguan, *Appl. Catal., B*, 2018, **238**, 465–470.
73 Q. Han, B. Wang, J. Gao, Z. Cheng, Y. Zhao, Z. Zhang and L. Qu, *ACS Nano*, 2016, **10**, 2745–2751.
74 H. Yu, R. Shi, Y. Zhao, T. Bian, Y. Zhao, C. Zhou, G. I. N. Waterhouse, L. Wu, C. Tung and T. Zhang, *Adv. Mater.*, 2017, **29**, 1605148.
75 L.-L. Liu, F. Chen, J.-H. Wu, M.-K. Ke, C. Cui, J.-J. Chen and H.-Q. Yu, *Appl. Catal., B*, 2022, **302**, 120845.
76 C. Liu, W. Ma, J. Chen, Z. Mao and D. Wang, *J. Mater. Sci.: Mater. Electron.*, 2021, **32**, 25033–25044.
77 H. Shi, S. Long, J. Hou, L. Ye, Y. Sun, W. Ni, C. Song, K. Li, G. G. Gurzadyan and X. Guo, *Chem. – Eur. J.*, 2019, **25**, 5028–5035.
78 W. Tu, Y. Xu, J. Wang, B. Zhang, T. Zhou, S. Yin, S. Wu, C. Li, Y. Huang, Y. Zhou, Z. Zou, J. Robertson, M. Kraft and R. Xu, *ACS Sustainable Chem. Eng.*, 2017, **5**, 7260–7268.
79 F. Longobardo, G. Gentile, A. Criado, A. Actis, S. Colussi, V. Dal Santo, M. Chiesa, G. Filippini, P. Fornasiero, M. Prato and M. Melchionna, *Mater. Chem. Front.*, 2021, **5**, 7267–7275.
80 Z. Yang, D. Chu, G. Jia, M. Yao and B. Liu, *Appl. Surf. Sci.*, 2020, **504**, 144407.
81 Y. Zheng, Y. Luo, Q. Ruan, J. Yu, X. Guo, W. Zhang, H. Xie, Z. Zhang, J. Zhao and Y. Huang, *J. Colloid Interface Sci.*, 2022, **609**, 75–85.
82 P. Praus, L. Řeháčková, J. Čížek, A. Smýkalová, M. Koštejn, J. Pavlovský, M. F. Edelmannová and K. Kočí, *Sci. Rep.*, 2022, **12**, 13622.
83 G. Dong, D. L. Jacobs, L. Zang and C. Wang, *Appl. Catal., B*, 2017, **218**, 515–524.
84 H. Sun, Y. Cao, L. Feng and Y. Chen, *Sci. Rep.*, 2016, **6**, 22808.
85 E. Mitchell, A. Law and R. Godin, *J. Photochem. Photobiol., C*, 2021, **49**, 100453.
86 P. Strak, K. Koronski, K. Sakowski, K. Sobczak, J. Borysiuk, K. P. Korona, P. A. Dróżdż, E. Grzanka, M. Sarzynski, A. Suchocki, E. Monroy, S. Krukowski and A. Kaminska, *J. Alloys Compd.*, 2020, **823**, 153791.
87 S. Cao, H. Li, T. Tong, H. Chen, A. Yu, J. Yu and H. M. Chen, *Adv. Funct. Mater.*, 2018, **28**, 1802169.
88 P. Chaluvachar, Y. N. Sudhakar, G. T. Mahesha, V. G. Nair, N. Desai and D. K. Pai, *J. Energy Chem.*, 2025, **103**, 498–524.
89 J. A. Willms, H. Gleich, M. Schrempp, D. Menche and M. Engeser, *Chem. – Eur. J.*, 2018, **24**, 2663–2668.
90 M. Rueping, S. Zhu and R. M. Koenigs, *Chem. Commun.*, 2011, **47**, 8679–8681.
91 K. Tran, G. L. Beutner, M. Schmidt, J. Janey, K. Chen, V. Rosso and M. D. Eastgate, *J. Org. Chem.*, 2015, **80**, 4994–5003.
92 F. Pertusati and C. McGuigan, *Chem. Commun.*, 2015, **51**, 8070–8073.
93 P. Du, J. Schneider, G. Luo, W. W. Brennessel and R. Eisenberg, *Inorg. Chem.*, 2009, **48**, 4952–4962.
94 Z. Eroglu, B. Sündü and O. Metin, *Mater. Today Sustain.*, 2023, **23**, 100418.

95 Z. Eroglu and O. Metin, *ACS Appl. Nano Mater.*, 2023, **6**, 7960–7974.
96 A. Basak, M. S. Ozer, Z. Eroglu, K. Sun and O. Metin, *Langmuir*, 2025, **41**, 13381–13394.
97 O. Fónagy, E. Szabó-Bárdos and O. Horváth, *J. Photochem. Photobiol., A*, 2021, **407**, 113057.
98 L. Li, C. Hao, R. Zhai, W. He and C. Deng, *Fuel*, 2023, **331**, 125853.
99 S. T. Gebre, L. M. Kiefer, F. Guo, K. R. Yang, C. Miller, Y. Liu, C. P. Kubiak, V. S. Batista and T. Lian, *J. Am. Chem. Soc.*, 2023, **145**, 3238–3247.
100 T. T. D. Nguyen, D. Nguyen, P. P. Vo, H. N. Doan, H. T. N. Pham, V. H. Hoang, K. T. Le, K. Kinashi, V. T. Huynh and P. T. Nguyen, *J. Mol. Liq.*, 2023, **381**, 121831.
101 A. Gottuso, F. Parisi, D. Lenaz and F. Parrino, *J. Photochem. Photobiol., A*, 2024, **457**, 115871.
102 D. P. Hari and B. König, *Org. Lett.*, 2011, **13**, 3852–3855.
103 W. Han, P. Mayer and A. R. Ofial, *Adv. Synth. Catal.*, 2010, **352**, 1667–1676.
104 D. Gunasekera, J. P. Mahajan, Y. Wanzi, S. Rodrigo, W. Liu, T. Tan and L. Luo, *J. Am. Chem. Soc.*, 2022, **144**, 9874–9882.
105 W. J. Yoo and S. Kobayashi, *Green Chem.*, 2014, **16**, 2438–2442.
106 K. Luo, W.-C. Ang and L. Wu, *Asian J. Org. Chem.*, 2017, **6**, 50–367.